ACS OMEGA

Article

Cite This: ACS Omega 2019, 4, 22008−22020

http://pubs.acs.org/journal/acsodf

Arsenic(III) Removal by Nanostructured Dialdehyde Cellulose−Cysteine Microscale and Nanoscale Fibers

Hui Chen,[†] Sunil K. Sharma,[†] Priyanka R. Sharma,[†] Heidi Yeh, Ken Johnson, and Benjamin S. Hsiao*

Department of Chemistry, Stony Brook University, Stony Brook, New York 11794, United States

Supporting Information

ABSTRACT: Arsenite (As(III)) contamination in drinking water has become a worldwide problem in recent years, which leads to development of various As(III) remediation approaches. In this study, two biomass-based nanostructured materials, microscale dialdehyde cellulose−cysteine (MDAC−cys) and nanoscale dialdehyde cellulose−cysteine (NDAC−cys) fibers, have been prepared from wood pulp. Their As(III) removal efficiencies and mechanism were determined by combined adsorption, atomic fluorescence spectrometry, microscopy (scanning electron microscopy, transmission electron microscopy, and atomic force microscopy), and spectroscopy (Fourier transform infrared, ^{13}C CPMAS NMR) methods. The adsorption results of these materials could be well described by the Freundlich isotherm model, where the maximum adsorption capacities estimated by the Langmuir isotherm model were 344.82 mg/g for MDAC−cys and 357.14 mg/g for NDAC−cys, respectively. Both MDAC−cys and NDAC−cys materials were further characterized by X-ray diffraction and thermogravimetric analysis, where the results indicated that the thiol groups (the S content in MDAC−cys was 12.70 and NDAC−cys was 17.15%) on cysteine were primarily responsible for the adsorption process. The nanostructured MDAC−cys system appeared to be more suitable for practical applications because of its high cost-effectiveness.

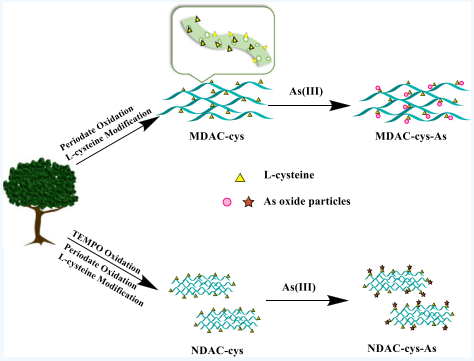

INTRODUCTION

Arsenic is a toxic and carcinogenic element that exists in several forms in atmosphere, soils, and water.[1−4] As drinking water is the most direct pathway for people to intake arsenic, high arsenic concentration in water supplies in some regions has become a major public health issue.[5−7] The chronic arsenic ingestion can cause skin cancer, bladder cancer, and kidney cancer, whereas acute arsenic exposure can lead to black foot disease, immunological system disorders, spontaneous pregnancy loss, and respiratory complications.[8,9] Because of both chronic and acute health threats on the human body, the limited arsenic concentration of 10 ppb in drinking water has been stipulated by the World Health Organization (WHO) in 2011.[10]

In nature, arsenate (As(V)) and arsenite (As(III)) are two most common forms of arsenic[11] in contaminated water. Compared with As(V), As(III) is more resistant and has higher health risks upon exposure. As a result, As(III) removal from water has been of more urgent need.[12−15] Currently, numerous methods for As(III) removal from drinking water have been reported. These methods include the approaches of precipitation/coagulation,[16] membrane separation,[17−19] ion exchange,[20] and adsorption.[21] Among these methods, adsorption is an appealing approach because of its low cost, high efficiency, relatively low energy consumption, and versatility for different water treatments.[9,22,23] In the current literature, iron oxides, activated alumina, and activated carbon are the most commonly used adsorbents for arsenic removal.[11,24−26] However, these adsorbents also possess different challenges such as complicated preparation procedures,[24,27] inconvenience in usage,[26] high preparation cost,[27] and low biocompatibility that could lead to serious secondary contamination in treated water.[28] As a result, there is still a need to develop more environmentally friendly, sustainable, and low cost adsorbent materials that can avoid some of the abovementioned problems but still be effective to treat As(III)-contaminated water, which forms the base for this study.

Cellulose is the most abundant and renewable natural polymer in the world and is an ideal source to extract water purification materials in a large scale at low cost.[28,29] Some examples of using cellulose-based materials to remove toxic metal ions from water are as follows. Succinic anhydride-modified nanocellulose has been shown to be effective to remove heavy metal ions (e.g., Cr(VI) and Pd(II)) and dyes[30,31] from water. Carbon aerogel prepared from microcrystalline cellulose has also been proven as an effective medium for removal of Cr(V) and Pb(II) ions.[32] The oxidized form of nanocellulose, such as carboxylated cellulose nanofiber (CNF), was found to possess excellent adsorption capability against uranium ions (UO_2^{2+}),[33,34] Pb(II) ions,[35] and Cd(II) ions.[36] Ferric hydroxide-coated CNFs have also been shown as a good adsorbent to remove phosphate from wastewater.[37] In

Received: September 19, 2019
Accepted: November 25, 2019
Published: December 10, 2019

DOI: 10.1021/acsomega.9b03078
ACS Omega 2019, 4, 22008−22020

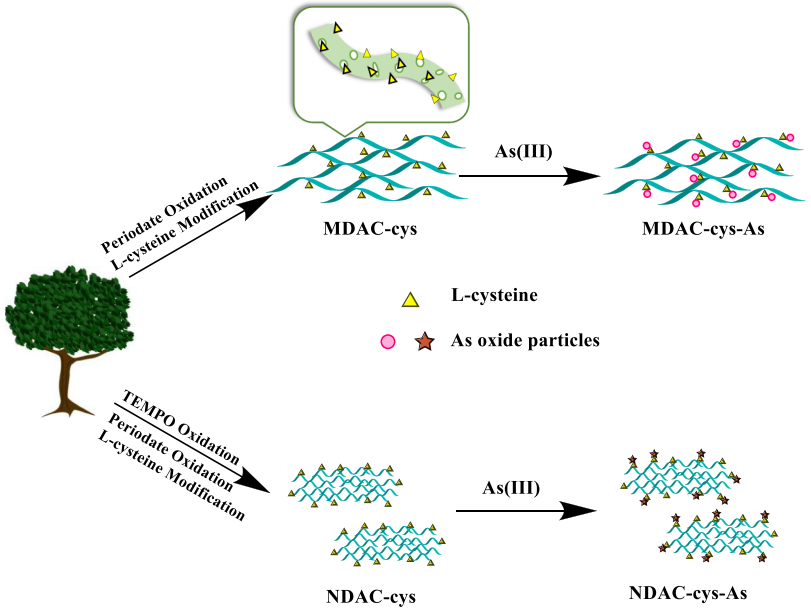

Figure 1. Pathways of the As(III) removal from water by MDAC−cys and NDAC−cys.

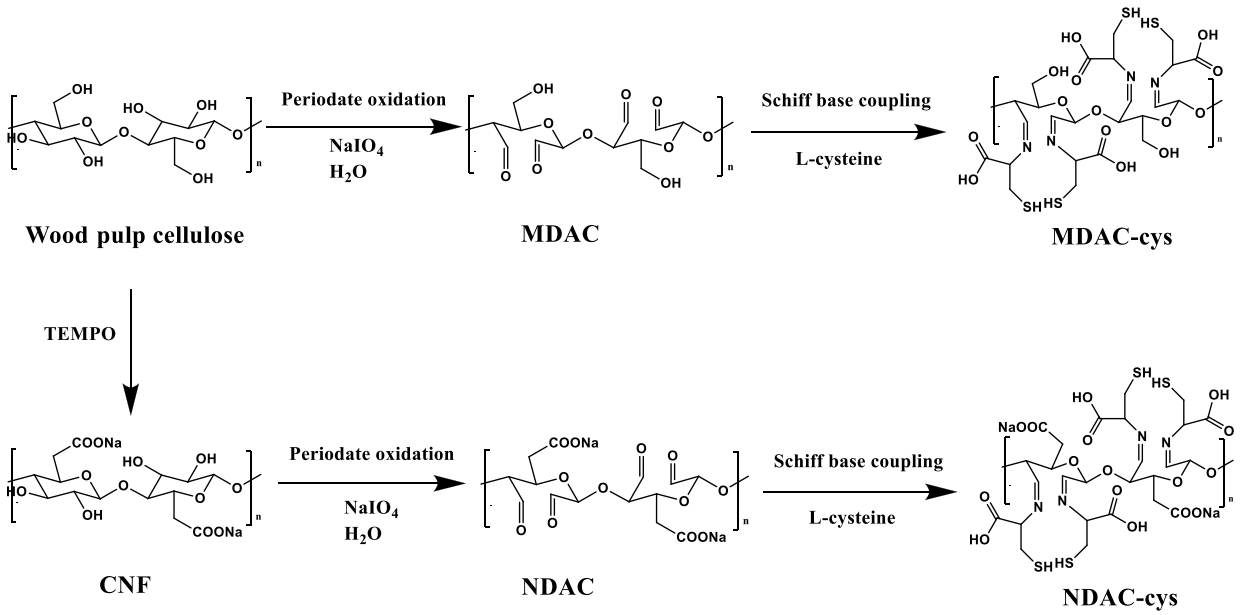

Figure 2. Synthesis routes of MDAC−cys and NDAC−cys.

addition, three-dimensional porous cellulose was found to be an effective adsorbent with high capacity to remove cationic dyes.[38] Recently, we further demonstrated that nanocomposites based on zinc oxide nanocrystal decorated regenerated microfibrillated cellulose have very high maximum capacity for As(V) removal.[39]

For As(III) removal, our previous work using thiol-functionalized chitin nanofibers only showed a medium removal efficiency (the maximum adsorption capacity was 149 mg/g at pH = 7.0).[40] In this study, we have designed a new adsorbent system containing higher concentration of thiol groups, based on the cellulose scaffold extracted from wood pulp, to improve the As(III) removal efficiency. These adsorbents can be prepared from any biomass in nature, thus representing a sustainable and potential low cost pathway for arsenic remediation.

To prepare the new absorbent system, two routes were carried out, leading to generation of nanostructured fibrous scaffolds at different scales (micro and nano). The schematic diagram of these two routes is shown in Figure 1. For the preparation of microscale scaffold, C_2-C_3 bonds in cellulose were selectively oxidized by sodium periodate to yield microscale dialdehyde cellulose (MDAC), where two aldehyde groups were formed at C_2 and C_3 positions of the anhydroglucose unit on the cellulose surface.[41,42] This oxidation process could cause significant changes in the properties of microscale cellulose, such as the decrease in crystallinity.[43,44] The Schiff-base MDAC and the cysteine complex (MDAC−cys) was further prepared by reacting MDAC with L-cysteine (i.e., through the nucleophilic reaction between aldehyde groups on MDAC and amino groups on L-cysteine[45]). It has been shown that during water treatment, the

DOI: 10.1021/acsomega.9b03078
ACS Omega 2019, 4, 22008−22020

thiol group in cysteine can bind to the As(III) ion through the complexation reaction because As(III) has high affinity for sulfur-containing ligands.[31,46−48] For the nanoscale scaffold, carboxylated CNFs were prepared first by TEMPO-mediated oxidation,[49] which converted the primary hydroxyl group to carboxyl group at the C_6 position in the anhydroglucose unit, enabling the cellulose surface to be negatively charged. The repulsive forces due to the charged surface would facilitate the defibrillation process. It has been shown that the TEMPO-mediated oxidation method is an effective approach to extract CNFs from the cellulose component of biomass (i.e., free of lignin and hemicellulose).[50−54] To prepare the nanoscale dialdehyde cellulose (NDAC)−cys complex adsorbent, the same reaction conditions for MDAC−cys were also used. CNFs were further oxidized by sodium periodate to produce NDAC, which was subsequently reacted with L-cysteine (i.e., by the nucleophilic reaction between aldehyde groups and amino groups).[45] Thus, the main difference between MDAC−cys and NDAC−cys should be the size of the fiber in the scaffold, where both surfaces contain thiol groups, capable of interacting with As(III) ions.

RESULTS AND DISCUSSION

Characterization of MDAC−cys and NDAC−cys Complexes. The synthesis routes for MDAC−cys and NDAC−cys samples are illustrated in Figure 2, respectively. In the microscale route, the MDAC sample was prepared directly from the wood pulp cellulose fiber. The content of the aldehyde group in resulting MDAC was determined to be 11.23 mmol/g using the hydroxylamine hydrochloride titration method (procedures and calculation are presented in Table S1, Supporting Information). Subsequently, L-cysteine ($HO_2CCH(NH_2)CH_2SH$) was attached to MDAC using the Schiff-base reaction between aldehyde (on MDAC) and amine groups (on cysteine) to create the MDAC−cys complex. The final sample possessed the appearance of a microscale fiber, although each fiber was partially fibrillated and contained a large surface to volume ratio in water.

In the nanoscale route, the starting scaffolding material was CNFs. The content of carboxyl groups on the surface of CNFs, NDAC, and NDAC−cys were first measured using the conductometric titration method.[55] The degree of oxidation in the formation of carboxyl content for CNFs, NDAC, and NDAC−cys is illustrated in Table 1 (the initial conductometric titration results to determine the carboxyl content are shown in Figure S1 and Table S2 in Supporting Information). It was found that the COOH content on the CNF surface decreased with the subsequent periodate oxidation to produce NDAC. This can be attributed to the degradation of nanocellulose fibers during oxidation, which most likely occurred at the position close to the oxidized anhydroglucose units.[56−58] As a result, the resulting NDAC possessed less carboxyl content after the periodate treatment. This reaction also affected NDAC's aldehyde content, which was 7.25 mmol/g (Table S1), significantly lower than that of MDAC. During the cysteine modification on NDAC, the thiol and carboxyl functional groups in cysteine were introduced without further chemical changes. Therefore, the content of the carboxyl group in NDAC−cys was found to increase significantly because of the presence of cysteine which also has carboxyl groups (the results are shown in Table 1). Similar observations were also made by ^{13}C CPMAS NMR measurements, which will be discussed later.

Table 1. Degree of Oxidation of CNFs, NDAC, and NDAC−cys

	content of COOH group (mmol/g)
CNF−wood pulp	1.61
NDAC	0.97
NDAC−cys	3.81

Functionalization of cysteine was investigated by determining the carbon (C), sulfur (S), and nitrogen (N) composition in MDAC−cys and NDAC−cys using the elemental analysis (Thermo Finnigan, FLASH EA 1112) method, where the results are shown in Table 2. For MDAC−cys, the S content was 12.70%, which indicated 0.479 g/g of cysteine was attached on MDAC, while the S content in NDAC−cys was 17.15% and as a result, the cysteine content in NDAC−cys was 0.648 g/g. The cysteine content in NDAC−cys was higher than that in MDAC−cys, indicating that NDAC−cys should be a more effective adsorbent to remove As(III). However, it was also interesting to note that even MDAC−cys was in the microfiber form (fiber diameter about 30 μm), and its total functionalized surface area for L-cysteine attachment was in a similar range as that of the NDAC−cys nanofiber (fiber diameter about 5 nm). This indicated that the MDAC−cys microfiber was partially defibrillated by the periodate oxidation reaction and contained a great deal of inner surface region available for functionalization.

Table 2. The Elemental Analysis Results for MDAC−cys and NDAC−cys

	MDAC−cys	NDAC−cys
C (%)	38.52	25.95
N (%)	5.512	8.276
S (%)	12.70	17.15

The Fourier transform infrared (FTIR) spectra of wood pulp cellulose, MDAC, MDAC−cys, and pure cysteine are illustrated in Figure 3(i). In the spectrum of untreated wood pulp cellulose (Figure 3(i)a), two distinctive 3340 and 2900 cm^{-1} peaks were seen, which could be assigned to the −OH stretching and C−H symmetrical stretching in cellulose, respectively. In the spectrum of MDAC (Figure 3(i)b), the peaks at 1730 and 880 cm^{-1} could be attributed to the carbonyl groups and hemi-acetal units in cellulose, respectively. These peaks confirmed the formation of dialdehyde cellulose.[59,60] After the cysteine attachment, the 1730 cm^{-1} peak became more distinct (Figure 3(i)c), which could be attributed to the formation of carboxyl groups, verifying the creation of MDAC−cys.[41,61] Notably, MDAC and MDAC−cys still possessed the 3340 cm^{-1} peak because of the −OH stretching. However, the intensity of this peak decreased as a result of the decreases in hydroxyl groups at the C_2 and C_3 position for both MDAC and MDAC−cys. Similarly, the peak at 2900 cm^{-1}, corresponding to the C−H stretching, were present in both MDAC and MDAC−cys, but their intensities became much lower than that of wood pulp cellulose. This is because during the conversion of cellulose to MDAC−cys, the hydroxyl groups at C_2 and C_3 positions were first converted into aldehyde groups and then to imine groups. Finally, the peak at 1640 cm^{-1} was seen in MDAC−cys, which could be assigned to the C=N stretching.[62]

DOI: 10.1021/acsomega.9b03078
ACS Omega 2019, 4, 22008−22020

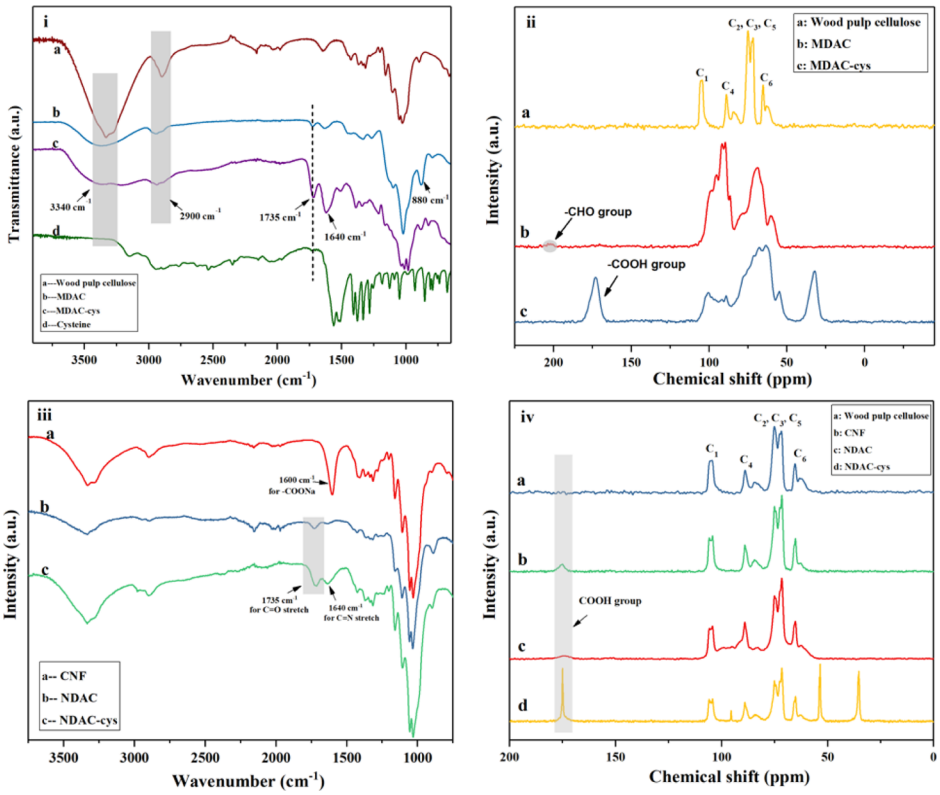

Figure 3. (i) FTIR spectra of (a) wood pulp cellulose, (b) MDAC, (c) MDAC−cys, and (d) cysteine; (ii) ^{13}C CPMAS NMR of (a) wood pulp cellulose, (b) MDAC, and (c) MDAC−cys; (iii) FTIR spectra of (a) CNF, (b) NDAC, and (c) NDAC−cys; (iv) ^{13}C CPMAS NMR spectra of (a) wood pulp cellulose, (b) CNF, (c) NDAC, and (d) NDAC−cys.

The solid state ^{13}C CPMAS NMR spectra of wood pulp cellulose, MDAC, and MDAC−cys are shown in Figure 3(ii). In the spectrum of wood pulp (Figure 3(ii)a), the signal at 66 ppm could be assigned to the carbon at the C_6 position. The doublets between 70 and 80 ppm could be assigned to the C_2, C_3, and C_5 carbons. The peak at 89 ppm was because of the C_4 carbon, and the peak between 100 and 110 ppm was associated with the anomeric carbon at C_1.[63,64] After the periodate oxidation, the peak around 201 ppm was observed, corresponding to the aldehyde group in MDAC at C_2 and C_3 positions. Typically, the peak related to the aldehyde group in cellulose is difficult to detect by NMR because of the conversion of the dialdehyde group to the acetal form. The sharper peaks in the NMR spectrum of wood pulp cellulose were because of the high degree of crystallinity, which was also supported by the wide-angle X-ray diffraction (WAXD) data to be discussed later. The periodate oxidation treatment was found to be able to profoundly decrease the crystallinity of cellulose, resulting in low crystallinity MDAC with a broad NMR spectrum,[41] which was also confirmed by WAXD. In the spectra of Figure 3(ii)b (MDAC), the C_2, C_3, and C_5 regions were found to merge together, which was also the case of MDAC−cys (Figure 3(ii)c). However, in the MDAC−cys spectrum, a distinct peak at 173 ppm was seen, which could be attributed to the carboxyl group in cysteine. New peaks at 31 and 58 ppm could be attributed to the backbone carbon and side chain carbon in cysteine, respectively. It is clear that the ^{13}C CPMAS NMR results confirmed the synthesis of the MDAC−cys complex and the further decrease in cellulose crystallinity during the Schiff-base reaction. The summary of the characteristic ^{13}C CPMAS NMR peaks in wood pulp cellulose, MDAC, and MDAC−cys is presented in Table S3 in Supporting Information.

The FTIR spectra of CNFs, NDAC, and NDAC−cys are shown in Figure 3(iii). In the spectrum of CNFs, the peak appeared at 1600 cm^{-1} could be attributed to the −COONa stretch induced by the TEMPO oxidation process. After periodate oxidation, the distinctive peak at 1730 cm^{-1} showed up which indicated the presence of carbonyl groups in NDAC. In the spectrum of NDAC−cys, the peak at 1730 cm^{-1} became more intense after the cysteine attachment, whereas the peak at 1640 cm^{-1} (C═N stretch) was also observed, indicating the formation of NDAC−cys.

The ^{13}C CPMAS NMR spectra for CNFs, NDAC, and NDAC−cys were also collected and the results are shown in Figure 3(iv). This figure also included the cellulose spectrum with the peaks in the range from 60 to 110 ppm marked as references. In Figure 3(iv)b, the appearance of the 175 ppm peak clearly indicated the presence of the carboxyl group in TEMPO-oxidized CNFs. It was found that TEMPO-mediated oxidation did not severely decrease the crystallinity of cellulose because the general feature of the peaks in the spectrum remained sharp. When CNFs were converted to NDAC by periodate oxidation, the 175 ppm peak was found to decrease notably (Figure 3(iv)c), indicating that the carboxyl content in NDAC became lower than that in CNFs. This was consistent with the titration results shown in Table 1. It was found that the overall crystallinity in NDAC remained higher even though the periodate oxidation process had a great tendency to degrade the cellulose chains. In NDAC−cys (Figure 3(iv)d), the intensity of the peak at 175 ppm because of the carboxyl group, as well as those of the peaks at 31 and 58 ppm,

DOI: 10.1021/acsomega.9b03078
ACS Omega 2019, 4, 22008−22020

increased sharply. This was because of the presence of cysteine molecules, not from the cellulose entity. The overall crystallinity of NDAC−cys was still high after the Schiff-base reaction (Table 3).

Table 3. Comparison of the Maximum As(III) Adsorption Capacity Estimated by the Langmuir Isotherm Model for Different Adsorbents

adsorbents	As(III) adsorption capacity (mg/g)	references
activated carbon (coconut)	146.3	79
ferrihydrite	266.5	81
CuO−Fe_3O_4 nanoparticles	118.11	83
Fe(III)−Ti(IV) binary oxide	85.13	80
Fe_3O_4−MnO_2 nanoplates	72.83	82
thiol resin dry powder	30	84
thiol chitosan bead	2.5	9
thiol-modified chitin nanofiber	149	40
Fe(III)-loaded resins	63	85
MDAC−cys	344.82	this study
NDAC−cys	357.14	this study

Structure and Morphology of MDAC−cys and NDAC−cys and Their As(III)-Adsorbed Composites. The surface morphology of MDAC−cys and NDAC−cys complexes before and after the As(III) adsorption was carried out by scanning electron microscopy/energy dispersive spectroscopy (SEM/EDS) measurements, and the results are shown in Figures 4 and 5, respectively. All these images were collected using freeze-dried samples. In Figure 4, it was seen that wood pulp cellulose showed long and thick microscale fibers with an average diameter of 34 μm. However, after the periodate oxidation, MDAC fibers became thinner (with an average diameter of 30 μm), shorter, and more porous. From the solid sample, it was difficult to determine the true porosity of the microfiber. After the cysteine attachment, the overall morphology and the average diameter of MDAC−cys fibers remained the same as those of MDAC. This indicated that the majority of cysteine attachment took place inside the microfiber, which confirmed that the microfiber was partially defibrillated containing a high inner surface area. The morphology of the floc sample (MDAC−cys−As(III)-1500) prepared by adsorption of As(III) at 1500 ppm with MDAC−cys is shown in Figure 4d. It was seen that some portion of MDAC−cys became severely aggregated and covered by the As(III) layer. The corresponding EDS spectra of MDAC−cys and MDAC−cys−As(III)-1500 are shown in Figure 4e,f, respectively. The EDS spectrum of MDAC−cys−As(III)-1500 (Figure 4f) clearly illustrated the presence of high As content in the floc sample. The SEM image and element mapping spectra of the MDAC−cys−As(III)-500 sample prepared by

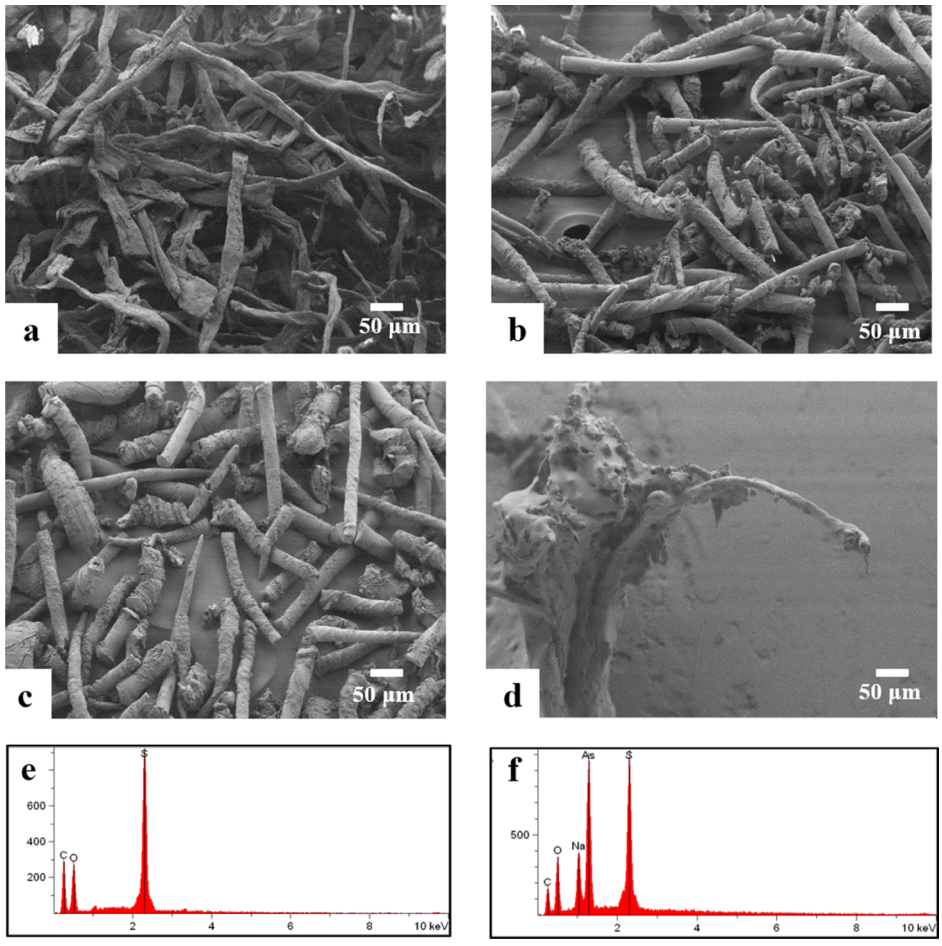

Figure 4. SEM images of (a) wood pulp cellulose, (b) MDAC, (c) MDAC−cys, and (d) MDAC−cys−As(III)-1500 (MDAC−cys adsorption with 1500 ppm of As(III)); element mapping spectra of (e) MDAC−cys and (f) MDAC−cys−As(III)-1500.

DOI: 10.1021/acsomega.9b03078
ACS Omega 2019, 4, 22008−22020

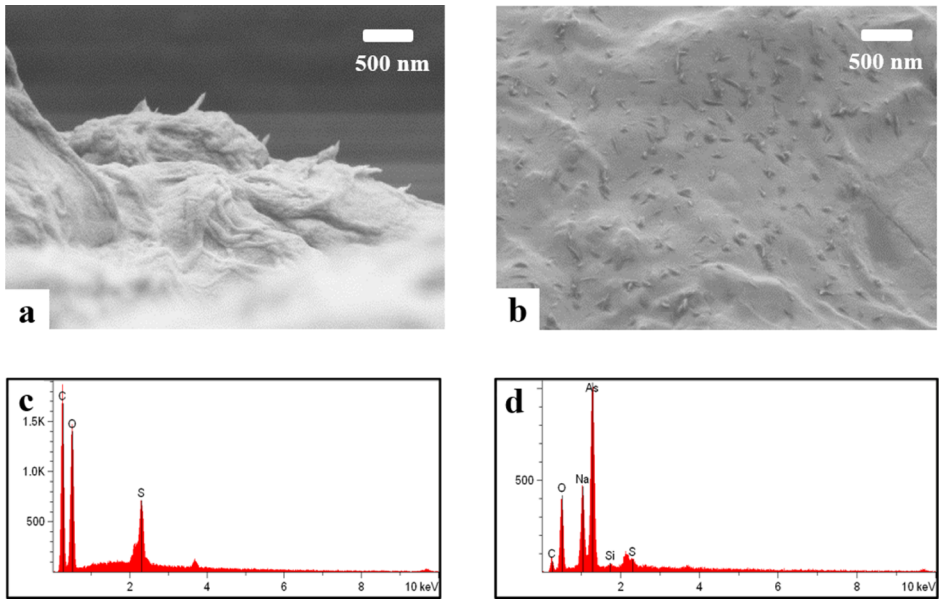

Figure 5. SEM images of (a) NDAC−cys and (b) NDAC−cys−As(III)-1500 (NDAC−cys adsorption with 1500 ppm of As(III)); element mapping spectra of (c) NDAC−cys and (d) NDAC−cys−As(III)-1500.

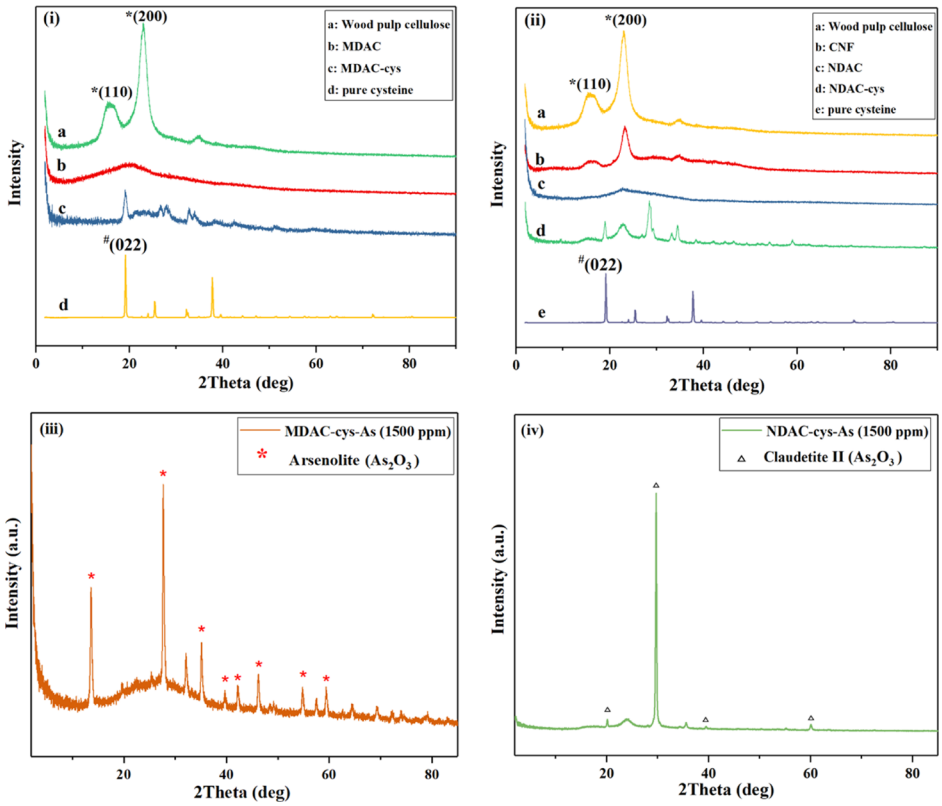

Figure 6. WAXD spectra of (i) (a) wood pulp cellulose, (b) MDAC, (c) MDAC−cys, and (d) cysteine; (ii) (a) wood pulp cellulose, (b) CNF, (c) NDAC, (d) NDAC−cys, and (e) cysteine; (iii) MDAC−cys−As(III) in 1500 ppm and (iv) NDAC−cys−As(III) in 1500 ppm.

adsorption of 500 ppm As(III) are shown in Figure S2 (Supporting Information) in which the overall morphology was found to be similar to that shown in Figure 4d, even though the As(III) content was 3 times less.

Figure 5 illustrates typical SEM images and corresponding EDS spectra of NDAC−cys NDAC−cys−As(III)-1500 samples. In NDAC−cys (Figure 5a), the SEM image showed strong fiber aggregation, where only bundles of aggregated nanofibers could be identified (the average bundle diameter was 70 nm). In Figure 5b, the SEM image indicated that the floc surface containing the matrix of NDAC−cys became relatively smooth (because of strong fiber aggregation), where the adsorbed As(III) formed nanoparticles dispersed quite uniformly on the floc surface. The EDS spectrum of NDAC−cys showed the appearance of C, O, and S peaks (S was due to the presence of cysteine), whereas the EDS spectrum of

DOI: 10.1021/acsomega.9b03078
ACS Omega 2019, 4, 22008−22020

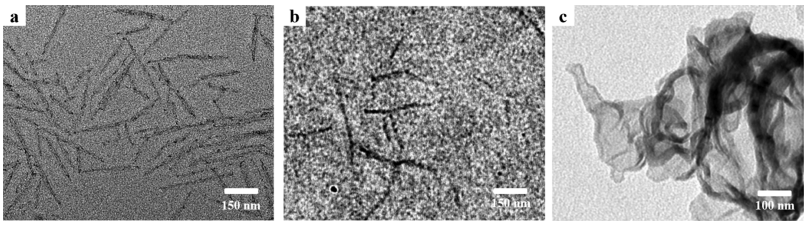

Figure 7. TEM images of (a) CNFs, (b) NDAC, and (c) NDAC−cys.

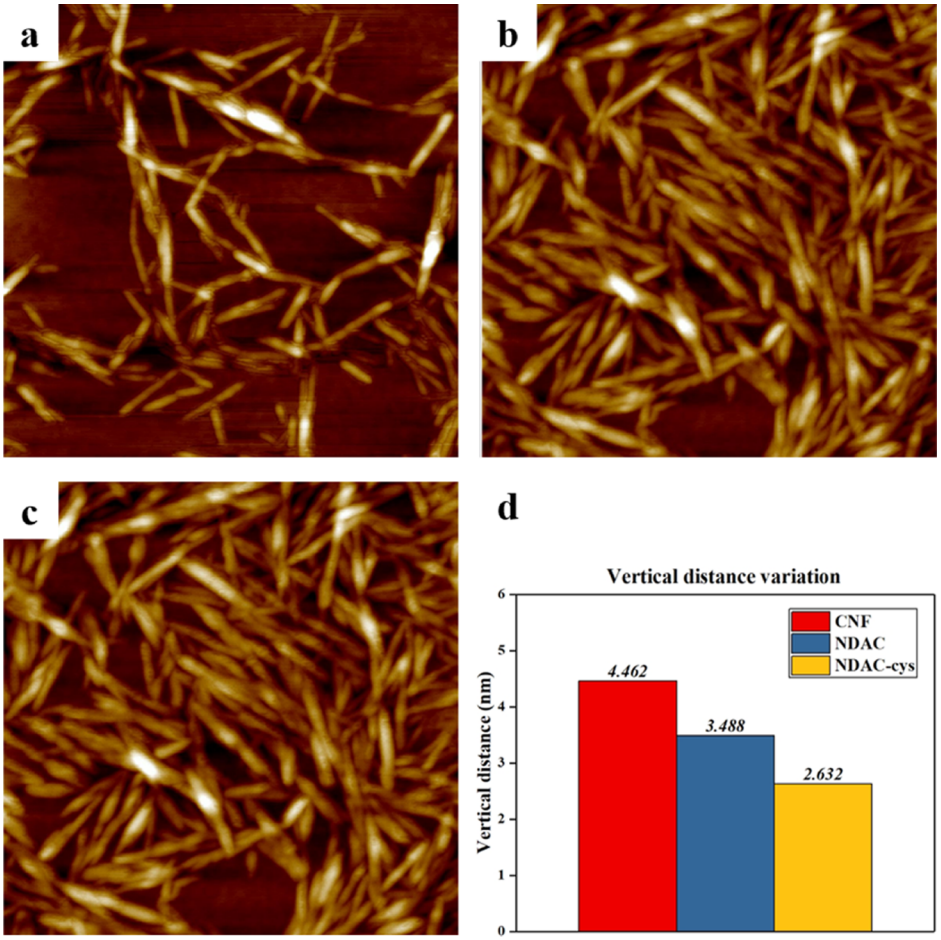

Figure 8. AFM images of (a) CNFs, (b) NDAC, (c) NDAC−cys, and (d) average height (vertical distance) determined from the AFM images.

NDAC−cys−As(III)-1500 floc showed a distinct As peak (the NDAC−cys−As(III)-500 floc prepared with 500 ppm of As(III) exhibited similar morphology and EDS results as shown in Figure S3, Supporting Information).

WAXD profiles of wood pulp cellulose, MDAC, MDAC−cys, and the reference compound (L-cysteine) are illustrated in Figure 6(i). It was seen that the WAXD profile of cellulose exhibited a relatively high crystallinity index (63.18%), based on the Segal empirical equation,[65] using the (002) crystalline peak at 22.5° and the amorphous background at 18° as the references. The equation is shown below (eq 1)

$$\mathrm{CrI} = (I_{22.5^\circ} - I_{18^\circ})/I_{22.5^\circ} \quad (1)$$

It was also found that after periodate oxidation, the crystallinity of MDAC disappeared almost completely (Figure 6(i)b). This observation was consistent with the ^{13}C CPMAS NMR results (Figure 3(ii)), where the relevant peaks to C_1, C_4, $C_{2,3,5}$, and C_6 has drastically broadened. The Brunauer−Emmett−Teller (BET) surface area result showed that MDAC has a surface area of 1.87 m^2/g (Figure S4). This value was comparable to that of NDAC (to be discussed later), confirming the nanostructured nature of the MDAC microfiber that are partially defibrillated. The WAXD profile of the MDAC−cys sample exhibited distinct diffraction peaks (Figure 6(i)c), which did not bear resemblance to pure L-cysteine crystals (Figure 6(i)d). We speculate that the molecular complexes between cysteine and the aldehyde group might form some form of crystal structure at a very small scale. The WAXD profile of MDAC−cys thus contained an amorphous cellulose background (MDAC) and diffraction from the crystal of cysteine-based molecular complexes. After As(III) adsorption, the MDAC−cys−As(III)-1500 floc samples exhibited the diffraction profile that could be indexed perfectly by the crystal of arsenolite (As_2O_3) as shown in Figure 6(iii).[66] This indicated that the presence of cysteine provided an effective adsorption site for the mineralization of As_2O_3 crystals. Based

DOI: 10.1021/acsomega.9b03078
ACS Omega 2019, 4, 22008−22020

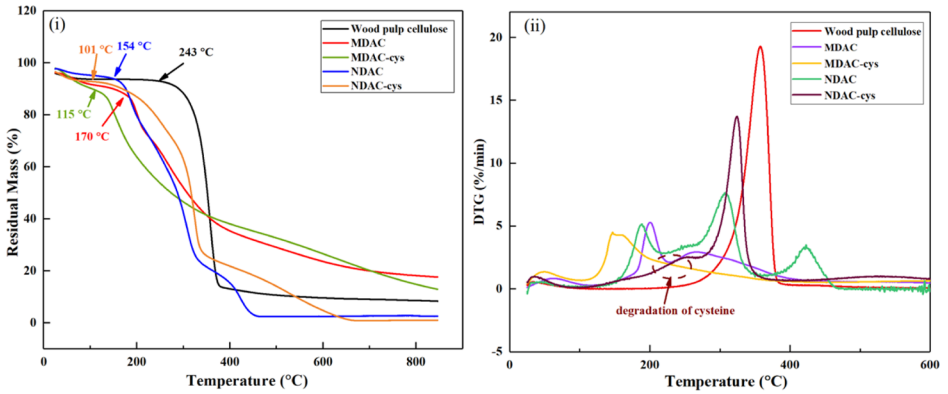

Figure 9. (i) TGA and (ii) DTG curves of cellulose, MDAC, MDAC−cys, NDAC, and NDAC−cys.

on the SEM image (Figure 4f), a thin layer of As_2O_3 crystals appeared on the surface of the MDAC−cys scaffold.

Figure 6(ii) illustrates the WAXD profiles of cellulose, NDAC, NDAC−cys, and L-cysteine. It was seen that the crystallinity index of CNFs was increased by the TEMPO oxidation method ($CI_{(CNF)}$ = 75%, Figure 6(ii)b), but the crystallinity index of NDAC was severely decreased by the periodate oxidation treatment as shown by the drastic decrease in the intensity of the (002) peak as shown in Figure 6(ii)c. The surface area of NDAC was determined to be 3.97 m^2/g from the BET surface measurement (Figure S4). However, the crystallinity index of NDAC was still larger than that of MDAC that was almost completely amorphous. The WAXD profile of NDAC−cys was very similar to that of MDAC−cys, but the former showed more distinct diffraction peaks, indicating the higher crystallinity in the cellulose scaffold and probably the larger size of the cysteine-based molecular complex crystal. The WAXD profile of NDAC−cys−As(III)-1500 shown in Figure 6(iv) could be indexed well by the claudetite II crystal, which is a polymorph of the As_2O_3 crystal.[67] However, severe peak broadening was seen in the diffraction profile of NDAC−cys−As(III)-1500, as compared with the profile of MDAC−cys−As(III)-1500. This indicated that the resulting crystal size (claudetite II) in NDAC−cys−As(III)-1500 was much smaller, which was consistent with the observation of As_2O_3 nanocrystal formation in Figure 5b.

The morphology of CNFs, NDAC, and NDAC−cys were also investigated by the transmission electron microscopy (TEM) technique. CNFs extracted by the TEMPO oxidation method exhibited an average width of 5 nm and an average length of 200 nm as illustrated in Figure 7a. After the periodate oxidation, the average length of NDAC decreased slightly (to 150 nm) but the average width remained the same. The decrease in the length of NDAC clearly indicated that the periodate oxidation process caused degradation in CNFs. The morphology of NDAC−cys suggested that the modification of cysteine seemed to cause some aggregation of nanofibers. This is not truly surprising as cysteine is a zwitterionic molecule, where the positively charged amine group can interact with the negatively charged carboxylate group on the CNFs and cause the CNFs to aggregate because of the screening effect.

The thicknesses of CNFs, NDAC, and NDAC−cys nanofibers were investigated by atomic force microscopy (AFM), and the results are shown in Figure 8. The AFM image of CNFs confirmed that the thickness of the extracted CNFs was 4−5 nm, in agreement with TEM results as well as previous literature.[68] This suggested that the cross-section of the TEMPO-oxidized CNF was a square shape. The periodate oxidation treatment clearly decreased the average fiber thickness to about 3.5 nm. The Schiff-base reaction further decreased the average fiber thickness to about 2.6 nm, even though the average width appeared to be the same.

Thermal Property. The thermogravimetric analysis (TGA) has been routinely used to investigate the thermal stability of the cellulose-based samples.[69] Figure 9(i) illustrates the TGA curves of cellulose, MDAC, MDAC−cys, NDAC, and NDAC−cys samples. The onset temperature, highest degradation temperature, and final residue percentage of these samples are listed in Table S4 (Supporting Information). One common feature in dehydration was observed in these samples. In this process, 0.55−1.22% of weight loss was observed in the temperature range between 25 and 100 °C. In wood pulp cellulose, the second weight loss started at 243 °C, which has often been considered as the primary cellulose structure degradation, and left behind 8.3% residue at 850 °C. These results are consistent with the literature data.[70] It is well known that the extensive hydrogen bonding between cellulose chains in the crystal structure can greatly increase the thermal stability, whereas the loss of crystallinity can also decrease the thermal stability.[71] This was certainly the case for MDAC, where degradation started at 170 °C. Furthermore, degradation of MDAC−cys commenced even at a lower temperature (115 °C), which was consistent with the loss of crystallinity as observed by NMR and WAXD techniques. It has been reported that L-cysteine starts to decompose at 250 °C,[72] which overlapped with the main degradation region of MDAC−cys. As a result, the degradation process of cysteine could not be observed very clearly even in derivative thermogravimetric (DTG) curves (Figure 9(ii)). It has been reported that the thermal degradation of TEMPO-oxidized CNFs started to occur at approximately 200 °C,[70] while for the original cellulose, degradation began at 243 °C. This is because the formation of sodium carboxylate groups led to a significant reduction in thermal stability.[73−75] NDAC appeared to decompose at around 154 °C, significantly lower than that of CNFs. Compared to NDAC, NDAC−cys thermal degradation started even at a lower temperature (around 101 °C), indicating that the thermal stability of NDAC−cys was the lowest among the tested samples.

The DTG curves of cellulose, MDAC, MDAC−cys, NDAC, and NDAC−cys are shown in Figure 9(ii), and the corresponding maximum degradation temperature of each sample is summarized in Table S3 (Supporting Information). Wood pulp cellulose exhibited a single peak with T_{max} at 355

DOI: 10.1021/acsomega.9b03078
ACS Omega 2019, 4, 22008−22020

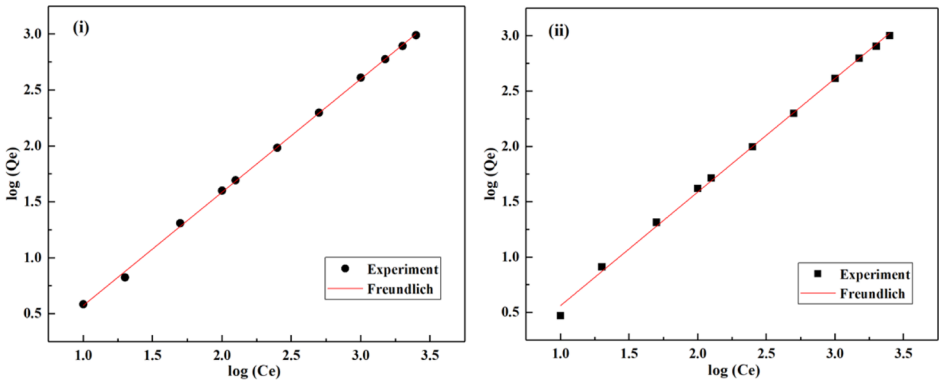

Figure 10. Fitting results using the Freundlich model for the As(III) adsorption data based on (i) MDAC−cys and (ii) NDAC−cys.

°C, which is related to the degradation of anhydroglucose units in the cellulose chain. DTG curves of MDAC exhibit a two-step degradation, corresponding to the degradation of anhydroglucuroaldhehye units at 200 °C[76] and the subsequent degradation of anhydroglucose units in the region between 229 and 400 °C. The first degradation of the anhydroglucuroaldhehye units indicated that the dialdehyde modification was randomly distributed in the cellulose chain. The MDAC−cys also showed two-step degradation with one small peak at 146 °C and one broad peak at 160 °C, covering the region between 160 and 383 °C. It has been reported that the maximum degradation for cysteine starts at 250 °C.[77] Hence, the broad peak between 160 and 383 °C could be attributed to the degradation of anhydroglucose units as well as anhydroglucose units bonded to the cysteine moiety. It was interesting to see that NDAC presented a three-peak degradation profile, having the peaks at 187, 306, and 422 °C, respectively. The degradation at 187 °C corresponded to the anhydroglucoronic units, the degradation peaks at 306 and 422 °C could be attributed to the anhydroglucose units in the cellulose chain in the amorphous and crystalline regions. The DTG curve for NDAC−cys also showed three degradation steps with peaks at 161, 249 (broad), and 324 °C, respectively. These peaks corresponded to the degradation processes of the anhydroglucuronic units, cysteine moiety, and anhydroglucose units, respectively.

Adsorption Efficiency against As(III). In order to investigate the adsorption efficiency of As(III) by MDAC−cys and NDAC−cys, a batch remediation experiment was conducted on simulated wastewater containing As(III) impurities. The simulated As(III)-contaminated water was prepared according to the method described in the Experimental Section. As(III) adsorption results using MDAC−cys and NDAC−cys as adsorbents are summarized in Tables S5 and S6 (Supporting Information). In these tables, the Q_e value (experimental adsorption capacity) was calculated as the product of adsorption efficiency and ideal adsorption capacity. The C_e value was taken as the equilibrium concentration of As(III). These results were analyzed by both the Langmuir and Freundlich models. The expression for the Langmuir model is shown in eq 2 and the corresponding Langmuir fitting curves for MDAC−cys and NDAC−cys are presented in Figure S5 (Supporting Information).

$$C_e/Q_e = C_e/Q_m + 1/Q_m \times K \quad (2)$$

where Q_m is the adsorption capacity of the adsorbent and K is a constant for the adsorbent in a chosen temperature.

We noticed that the Langmuir model could not fit the adsorption results for the entire As(III) concentration range (10−2500 ppm) with a good R^2 coefficient value. This is not surprising because the Langmuir model assumes the monolayer adsorption isotherm, which cannot account for the mineralization process of forming As_2O_3 crystals at the later stage. As a result, we used the Langmuir model to fit the results in two concentration ranges, where the first concentration range might meet the criteria of Langmuir adsorption and the analysis could lead to the estimate of the maximum adsorption capacity. The analysis was carried out as follows. At a very low concentration range (10−20 ppm), a very low adsorption efficiency was seen for both the samples (MDAC−cys: 60−70% and NDAC−cys: 59−82%). This indicated that the ionic bonding between As(III) and thiol group only took place partially, whereby the adsorption data was not used in the Langmuir analysis. At a higher concentration range (50−250 ppm), we believe that the ionic bonding between As(III) and the thiol group probably occurred fully, which would meet the assumption of the Langmuir model. This is certainly the case shown in Figure S5, where the Langmuir model could fit very well for both MDAC−cys and NDAC−cys systems with good R^2 coefficient values, that is, 0.943 and 0.815, respectively. The fitting results are summarized in Table S7 (Supporting Information), where the maximum adsorption capacity (Q_m) was found to be 344.82 mg/g for MDAC−cys and 357.14 mg/g for NDAC−cys. We also used the Langmuir model to fit the data in the concentration range of 500−2500 ppm (Figure S5) as the reference, where the poor R^2 coefficient values clearly indicate that the model fails when the mineralization process begins.

In contrast, we found that the Freundlich isotherm model could be used to fit the adsorption results for the entire As(III) concentration range (10−2500 ppm). The Freundlich isotherm model can be expressed as follows.

$$\log(Q_e) = \log(K_F) + 1/n \log(C_e) \quad (3)$$

where K_F and n are constants for a given adsorbate and adsorbent at the chosen temperature. The fitting results of the As(III) adsorption data by using the Freundlich model for MDAC−cys and NDAC−cys are shown in Figure 10(i) and Table S8 (Supporting Information). It was found that both fits were excellent with the R^2 coefficient value as high as 0.999 and 0.998 for MDAC−cys and NDAC−cys, respectively. These results are consistent with the fact that MDAC−cys and NDAC−cys are both complex and heterogenous systems, whereby their adsorption behavior is described by the

DOI: 10.1021/acsomega.9b03078
ACS Omega 2019, 4, 22008−22020

multilayer adsorption mechanism using the Freundlich isotherm model.[78]

With the Freundlich model analysis, the highest Q_e value obtained for MDAC−cys was 982 mg/g, when challenged with the 2500 ppm As(III) solution. However, the Q_e value obtained for MDAC−cys was only 3.58 mg/g for 10 ppm As(III) concentration. The drastic increase of the Q_e value of MDAC−cys with the increase in the concentration of As(III) is probably because of the occurrence of mineralization of As(III) at high concentration (>500 ppm). Similar results were obtained in previous studies involving the adsorption of lead, cadmium, and uranium ions using nitro-oxidized carboxycellulose.[34−36] The As(III) removal efficiency of NDAC−cys is very similar to that of MDAC−cys. The highest Q_e value obtained for NDAC−cys was 1011 mg/g when 2500 ppm As(III) concentration was used, while the lowest Q_e value was only 2.95 mg/g when 10 ppm As(III) concentration was present. Similar results between MDAC−cys and NDAC−cys indicated that at low As(III) concentrations, adsorption is the dominant mechanism for removal of As(III), while at high As(III) concentration (>500 ppm), mineralization becomes the dominant mechanism.

Comparison between MDAC−cys, NDAC−cys, and Other Adsorbents. The comparison of the maximum adsorption capacity (Q_m) from varying adsorbents is shown in Table 2. Is this table, the maximum adsorption capacity values (Q_m) for MDAC−cys and NDAC−cys were estimated using the adsorption data in the concentration range of 50−250 ppm, where the mineralization process did not take place. The calculated Q_m value of MDAC−cys is 344.82 mg/g and NDAC−cys is 357.14 mg/g, which are higher than most reported values. For example, activated coconut carbon[79] has a Q_m of 146.3 mg/g at 600 ppm, and Fe (III) particles,[80] Ferrihydrite,[81] and Fe_3O_4-based nanoparticles[82,83] have Q_m between 63 and 266 mg/g in a relatively narrow As(III) concentration range (1−50 ppm). There are also reports on As removal using thiol groups in functionalized materials such as thiol-modified chitosan beads[9] and chitin nanofibers.[40] However, these materials have only shown Q_m values between 2.5 and 149 mg/g, which are significantly lower than those of DAC−cys and NDAC−cys. Aided by the mineralization process, both MDAC−cys and NDAC−cys substrates have shown very high removal efficiency. For example, the removal efficiency is 982 mg/g for MDAC−cys and 1011 mg/g for MDAC−cys at 2500 ppm of As(III).

The similar As(III) removal efficiencies between MDAC−cys and NDAC−cys suggests that MDAC−cys is clearly a more practical and cost-effective system for As(III) remediation in water. In fact, there can be unique advantages of using the microfiber format of cellulose if the internal surface area in the scaffold is high (i.e., the fiber is partially defibrillated but still maintains the overall integrity). The advantages include the less processing steps with significant saving in chemicals, water, and energy, as well as the easy handling ability during the adsorption operation.

CONCLUSIONS

Two nanostructured cellulose-based adsorbents: MDAC−cys and NDAC−cys were demonstrated using wood pulp as the starting material. These two adsorbents exhibited similar but excellent As(III) removal efficiencies because of the small difference in the thiol (sulphur) content between MDAC−cys and NDAC−cys, which was about 12.70 and 17.15%, respectively. The slight decrease in the adsorption capacity of NDAC−cys for As(III) as compared to MDAC−cys could be because of the aggregation of NDAC−cys. The removal efficiencies of As(III) by MDAC−cys and NDAC−cys were found to increase with the As(III) concentration. At low As(III) concentrations (<500 ppm), the remediation process was dominated by the adsorption of As(III) on L-cysteine, while at high As(III) concentrations (>500 ppm), the remediation process was dominated by the mineralization of As(III) into As_2O_3 nanocrystals with different polymorphs (arsenolite on MDAC−cys and claudetite II on NDAC−cys). The adsorption results of MDAC−cys and NDAC−cys could be well described by the Freundlich isotherm model. However, their maximum adsorption capabilities were estimated using the data at the low concentration range (50−250 ppm): 344.82 mg/g for MDAC−cys and 357.14 mg/g for NDAC−cys. These values are significantly higher than all the reported values in the literature. The similar As(III) removal efficiencies between MDAC−cys and NDAC−cys suggests that the fabrication pathway based on the microfiber format is clearly a more practical and cost-effective means to produce biomass-based adsorbents for As(III) remediation in water.

EXPERIMENTAL SECTION

Materials. Cellulose derived from wood pulp was obtained from Georgia Pacific Ltd. USA. TEMPO reagent, sodium periodate ($NaIO_4$), hydroxylamine hydrochloride ($NH_2OH·HCl$), L-cysteine, sodium (meta)arsenite ($NaAsO_2$), sodium hydroxide (NaOH), sodium chlorite ($NaClO_2$), sodium hypochlorite (NaClO), and sodium bromide (NaBr) (analytical or reagent grade) were purchased from Sigma-Aldrich and used without further purification. Dialysis tubes (44 and 28 mm) with a molecular weight cut off (MWCO) of 6−8 kDa were obtained from Spectrum Laboratory BioTech. Deionized (DI) water was used in all the experimental procedures.

Preparation of MDAC. The preparation of MDAC was carried out using the method demonstrated by Lindh et al.[59] In this method, the wood pulp cellulose fiber was first grinded into a small length (<2 mm) using a microfine grinder analytical mill. Then, 5 g of the cellulose sample was suspended in 200 mL water to react with 1.3 times equivalent of $NaIO_4$ (8.25 g) for 16 h under vigorous stirring. To avoid decomposition of sodium periodate and photo oxidation, the reaction was carried out in dark throughout the preparation procedure. Temperature of the reaction mixture was maintained at 55 °C using a water bath. After the reaction, oxidized cellulose samples were filtered by a microfiltration filter and then purified thoroughly using a dialysis bag (MWCO: 6−8 kDa) in a 3 L water tank. DI water was changed frequently in this tank until the conductivity reached below 5 μS. A part of the product was freeze-dried for analysis.

Preparation of the MDAC−cys Complex. The MDAC−cys complex was prepared by a simple reaction as demonstrated previously.[40,41] In this preparation, 1 g of MDAC (dried weight) was suspended in 200 mL of water under constant stirring at 39 °C (in water bath). Then, 1.67 g of L-cysteine (2 equiv) was added into the MDAC suspension, where the suspension was stirred continuously for 5 h to complete the reaction. The final product was separated by microfiltration and purified by dialysis. Part of the MDAC−cysteine adsorbent sample was also freeze-dried for analysis.

Preparation of CNFs from Cellulose. CNFs were prepared by the TEMPO-mediated oxidation method as

DOI: 10.1021/acsomega.9b03078
ACS Omega 2019, 4, 22008−22020

follows.[49] 10 g of wood-based cellulose was first grinded into a small length (<2 mm) and the sample was then soaked in DI water (about 960 mL) overnight, followed by addition of sodium bromide (1.0 g) and the TEMPO agent (0.20 g). After 15 min of stirring, 100 mmoL of sodium hypochlorite solution (10 mmol per gram of cellulose) was added to initiate the oxidization process. The reaction was under mechanical stirring in a sealed bottle for 24 h at room temperature and the pH level was monitored and maintained around 10 by addition of 1 M NaOH solution. The reaction was then quenched using 4 mL ethanol. Subsequently, the oxidized cellulose sample was purified by dialysis with DI water, until the conductivity of water reached below 5 μS. The oxidized cellulose sample was further defibrillated using a homogenizer at 300 Pa for 10 min to obtain the CNF suspension. Part of the CNF sample was freeze-dried for further characterization.

Preparation of NDAC. NDAC was prepared by the periodate oxidation of CNFs. In brief, 5.28 g of $NaIO_4$ was added to 200 mL CNF suspension (1.6 wt %) at 55 °C using a water bath. The reacting mixture was stirred for 16 h in dark to complete the reaction. Subsequently, the product was purified by dialysis and then freeze-dried.

Preparation of the NDAC−cys Complex. The NDAC−cys complex was prepared by mixing L-cysteine (0.872 g, 2 equiv) with NDAC suspension (100 mL, 0.522 wt %) under stirring in a sealed bottle. After 5 h of reaction at 39 °C, the NDAC−cys product was formed, which was then purification by dialysis until the excess reactants were removed. Again, freeze-drying was used to prepare the solid NDAC−cys sample for the remediation test.

As(III) Remediation Study. For the As(III) remediation measurement, a series of As(III) solutions with different concentrations (10−2500 ppm) were made by diluting the 0.1 M $NaAsO_2$ stock solution with neutral DI water (pH ≈ 7). The remediation tests for both MDAC−cys and NDAC−cys were carried out by mixing 1 mg of freeze-dried powder sample with 2 mL of As(III) solution at different concentrations. After 24 h of contact time, the floc was formed and settled at the bottom of the test vial. Both the floc and upper layer supernatant were collected separately for characterizations.

Determine the Adsorption Capacity. The values of As(III) removal efficiency for both MDAC−cys and NDAC−cys samples were calculated based on the difference between the initial and final As(III) concentrations divided by the final As(III) concentration [measured by atomic fluorescence spectrometry (AFS)]. The ideal adsorption capacity of MDAC−cys and NDAC−cys were determined by the amount of As(III) (mg) in solution and the amount of MDAC−cys (g) and NDAC−cys (g) used in the experiment, assuming that MDAC−cys and NDAC−cys could remove all As(III) from the solution. The experimental adsorption capacity was the product of the percent efficiency and the ideal adsorption capacity.[34]

Sample Characterization Methods. The details of the varying characterization techniques are described in the Supporting Information. In brief, the mechanisms of the As(III) removal from water by MDAC−cys and NDAC−cys were investigated by FTIR spectroscopy (PerkinElmer Spectrum One), ^{13}C CPMAS nuclear magnetic resonance (NMR, Bruker Ultrashield 500 MHz), elemental analysis (Thermo Finnigan, Model FLASH EA 1112), thermogravimetric analysis (TGA, PerkinElmer STA-6000), SEM (Zeiss LEO 1550 SFEG-SEM) with EDS capability, TEM (FEI Tecnai G2 Spirit BioTwin), AFM (Bruker OTESPA tip 10 nm), BET surface (Quantachrome), and WAXD (Benchtop Rigaku MiniFlex 600) techniques. The supernatant from the remediation experiment was also characterized by the AFS (LUMINA 3300) technique. The dried floc samples were analyzed by FTIR, SEM, and wide-angle XRD measurements.

■ ASSOCIATED CONTENT

Supporting Information

The Supporting Information is available free of charge at https://pubs.acs.org/doi/10.1021/acsomega.9b03078.

Descriptions of sample characterization methods, including FTIR, ^{13}C CPMAS NMR, elemental analysis, TGA, SEM, TEM, AFM, BET surface measurement, wide-angle XRD, and AFS detection; determination of the aldehyde content; determination of the carboxyl group content; SEM image and element mapping of MDAC−cys−As(III)-500 and NDAC−cys−As(III)-500; BET surface adsorption of MDAC and NDAC; Langmuir adsorption isotherm model fitting for MDAC−cys and NDAC−cys in 50−250 and 500−2500 ppm, respectively; ^{13}C CPMAS NMR peaks in wood pulp, MDAC, and MDAC−cys samples; summary of TGA and DTG profiles; table of As(III) adsorption results by MDAC−cys and NDAC−cys (PDF)

■ AUTHOR INFORMATION

Corresponding Author

*E-mail: benjamin.hsiao@stonybrook.edu. Phone: +1(631) 632-7793.

ORCID

Hui Chen: 0000-0003-3337-0975

Benjamin S. Hsiao: 0000-0002-3180-1826

Author Contributions

†Authors H.C., S.K.S., and P.R.S. have equal contributions in this manuscript.

Notes

The authors declare no competing financial interest.

■ ACKNOWLEDGMENTS

The authors would like to thank the National Science Foundation (DMR-1808690) for the financial support of this study.

■ REFERENCES

(1) Jain, C. K.; Ali, I. Arsenic: occurrence, toxicity and speciation techniques. *Water Res.* **2000**, *34*, 4304−4312.

(2) Christoforidou, E. P.; Riza, E.; Kales, S. N.; Hadjistavrou, K.; Stoltidi, M.; Kastania, A. N.; Linos, A. Bladder cancer and arsenic through drinking water: A systematic review of epidemiologic evidence. *J. Environ. Sci. Health, Part A: Toxic/Hazard. Subst. Environ. Eng.* **2013**, *48*, 1764−1775.

(3) Wang, Y.; Ma, T.; Ryzhenko, B. N.; Limantseva, O. A.; Cherkasova, E. V. Model for the formation of arsenic contamination in groundwater. 1. Datong Basin, China. *Geochem. Int.* **2009**, *47*, 713−724.

(4) McGuigan, C. F.; Hamula, C. L. A.; Huang, S.; Gabos, S.; Le, X. C. A review on arsenic concentrations in Canadian drinking water. *Environ. Rev.* **2010**, *18*, 291−307.

(5) Neumann, A.; Kaegi, R.; Voegelin, A.; Hussam, A.; Munir, A. K. M.; Hug, S. J. Arsenic removal with composite iron matrix filters in Bangladesh: A field and laboratory study. *Environ. Sci. Technol.* **2013**, *47*, 4544−4554.

DOI: 10.1021/acsomega.9b03078
ACS Omega 2019, 4, 22008−22020

(6) Michael, H. A. An Arsenic Forecast for China. *Science* **2013**, *341*, 852.
(7) Martin, T. D.; Brockhoff, C. A.; Creed, J. T.; Long, S. E. Determination of metals and trace elements in water and wastes by inductively coupled plasma-atomic emission spectrometry. *Methods for Determination of Metals in Environmental Samples*; CRC Press Inc.: Boca Raton, 1992; pp 33−91.
(8) Wai, C. M.; Wang, J. S.; Yang, M. H. Arsenic contamination of groundwater, blackfoot disease, and other related health problems. *Biogeochemistry of Environmentally Important Trace Elements*; American Chemical Society, 2002; Vol. *835*, pp 210−231.
(9) Mohan, D.; Pittman, C. U. Arsenic removal from water/wastewater using adsorbents—A critical review. *J. Hazard. Mater.* **2007**, *142*, 1−53.
(10) Shrestha, R. R.; Shrestha, M. P.; Upadhyay, N. P.; Pradhan, R.; Khadka, R.; Maskey, A.; Maharjan, M.; Tuladhar, S.; Dahal, B. M.; Shrestha, K. Groundwater arsenic contamination, Its health impact and mitigation program in Nepal. *J. Environ. Sci. Health, Part A: Toxic/Hazard. Subst. Environ. Eng.* **2003**, *38*, 185−200.
(11) Dhoble, R. M.; Lunge, S.; Bhole, A. G.; Rayalu, S. Magnetic binary oxide particles (MBOP): A promising adsorbent for removal of As (III) in water. *Water Res.* **2011**, *45*, 4769−4781.
(12) Smedley, P. L.; Kinniburgh, D. G. A review of the source, behaviour and distribution of arsenic in natural waters. *Appl. Geochem.* **2002**, *17*, 517−568.
(13) Sharma, V. K.; Sohn, M. Aquatic arsenic: toxicity, speciation, transformations, and remediation. *Environ. Int.* **2009**, *35*, 743−759.
(14) Shan, C.; Tong, M. Efficient removal of trace arsenite through oxidation and adsorption by magnetic nanoparticles modified with Fe−Mn binary oxide. *Water Res.* **2013**, *47*, 3411−3421.
(15) Zhang, G.; Qu, J.; Liu, H.; Liu, R.; Wu, R. Preparation and evaluation of a novel Fe−Mn binary oxide adsorbent for effective arsenite removal. *Water Res.* **2007**, *41*, 1921−1928.
(16) Yamani, J. S.; Miller, S. M.; Spaulding, M. L.; Zimmerman, J. B. Enhanced arsenic removal using mixed metal oxide impregnated chitosan beads. *Water Res.* **2012**, *46*, 4427−4434.
(17) Akin, I.; Arslan, G.; Tor, A.; Cengeloglu, Y.; Ersoz, M. Removal of arsenate [As(V)] and arsenite [As(III)] from water by SWHR and BW-30 reverse osmosis. *Desalination* **2011**, *281*, 88−92.
(18) Gecol, H.; Ergican, E.; Fuchs, A. Molecular level separation of arsenic (V) from water using cationic surfactant micelles and ultrafiltration membrane. *J. Membr. Sci.* **2004**, *241*, 105−119.
(19) Figoli, A.; Cassano, A.; Criscuoli, A.; Mozumder, M. S. I.; Uddin, M. T.; Islam, M. A.; Drioli, E. Influence of operating parameters on the arsenic removal by nanofiltration. *Water Res.* **2010**, *44*, 97−104.
(20) Donia, A. M.; Atia, A. A.; Mabrouk, D. H. Fast kinetic and efficient removal of As(V) from aqueous solution using anion exchange resins. *J. Hazard. Mater.* **2011**, *191*, 1−7.
(21) Gupta, V. K.; Saini, V. K.; Jain, N. Adsorption of As(III) from aqueous solutions by iron oxide-coated sand. *J. Colloid Interface Sci.* **2005**, *288*, 55−60.
(22) Gu, Z.; Fang, J.; Deng, B. Preparation and evaluation of GAC-based iron-containing adsorbents for arsenic removal. *Environ. Sci. Technol.* **2005**, *39*, 3833−3843.
(23) O'Connell, D. W.; Birkinshaw, C.; O'Dwyer, T. F. Heavy metal adsorbents prepared from the modification of cellulose: A review. *Bioresour. Technol.* **2008**, *99*, 6709−6724.
(24) Chandra, V.; Park, J.; Chun, Y.; Lee, J. W.; Hwang, I.-C.; Kim, K. S. Water-dispersible magnetite-reduced graphene oxide composites for arsenic removal. *ACS Nano* **2010**, *4*, 3979−3986.
(25) Wu, Z.; Li, W.; Webley, P. A.; Zhao, D. General and controllable synthesis of novel mesoporous magnetic iron oxide@carbon encapsulates for efficient arsenic removal. *Adv. Mater.* **2012**, *24*, 485−491.
(26) An, B.; Liang, Q.; Zhao, D. Removal of arsenic(V) from spent ion exchange brine using a new class of starch-bridged magnetite nanoparticles. *Water Res.* **2011**, *45*, 1961−1972.
(27) Liu, R.; Shi, Y.; Wan, Y.; Meng, Y.; Zhang, F.; Gu, D.; Chen, Z.; Tu, B.; Zhao, D. Triconstituent Co-assembly to Ordered Mesostructured Polymer−Silica and Carbon−Silica Nanocomposites and Large-Pore Mesoporous Carbons with High Surface Areas. *J. Am. Chem. Soc.* **2006**, *128*, 11652−11662.
(28) Tian, Y.; Wu, M.; Lin, X.; Huang, P.; Huang, Y. Synthesis of magnetic wheat straw for arsenic adsorption. *J. Hazard. Mater.* **2011**, *193*, 10−16.
(29) Klemm, D.; Heublein, B.; Fink, H.-P.; Bohn, A. Cellulose: fascinating biopolymer and sustainable raw material. *Angew. Chem., Int. Ed.* **2005**, *44*, 3358−3393.
(30) Hokkanen, S.; Repo, E.; Sillanpää, M. Removal of heavy metals from aqueous solutions by succinic anhydride modified mercerized nanocellulose. *Chem. Eng. J.* **2013**, *223*, 40−47.
(31) Yang, R.; Aubrecht, K. B.; Ma, H.; Wang, R.; Grubbs, R. B.; Hsiao, B. S.; Chu, B. Thiol-modified cellulose nanofibrous composite membranes for chromium (VI) and lead (II) adsorption. *Polymer* **2014**, *55*, 1167−1176.
(32) Alatalo, S.-M.; Pileidis, F.; Mäkilä, E.; Sevilla, M.; Repo, E.; Salonen, J.; Sillanpää, M.; Titirici, M.-M. Versatile cellulose-based carbon aerogel for the removal of both cationic and anionic metal contaminants from water. *ACS Appl. Mater. Interfaces* **2015**, *7*, 25875−25883.
(33) Ma, H.; Hsiao, B. S.; Chu, B. Ultrafine cellulose nanofibers as efficient adsorbents for removal of UO_2^{2+} in Water. *ACS Macro Lett.* **2012**, *1*, 213−216.
(34) Sharma, P. R.; Chattopadhyay, A.; Sharma, S. K.; Hsiao, B. S. Efficient removal of UO_2^{2+} from water using carboxycellulose nanofibers prepared by the nitro-oxidation method. *Ind. Eng. Chem. Res.* **2017**, *56*, 13885−13893.
(35) Sharma, P. R.; Chattopadhyay, A.; Zhan, C.; Sharma, S. K.; Geng, L.; Hsiao, B. S. Lead removal from water using carboxycellulose nanofibers prepared by nitro-oxidation method. *Cellulose* **2018**, *25*, 1961−1973.
(36) Sharma, P. R.; Chattopadhyay, A.; Sharma, S. K.; Geng, L.; Amiralian, N.; Martin, D.; Hsiao, B. S. Nanocellulose from Spinifex as an effective adsorbent to remove cadmium(II) from water. *ACS Sustainable Chem. Eng.* **2018**, *6*, 3279−3290.
(37) Cui, G.; Liu, M.; Chen, Y.; Zhang, W.; Zhao, J. Synthesis of a ferric hydroxide-coated cellulose nanofiber hybrid for effective removal of phosphate from wastewater. *Carbohydr. Polym.* **2016**, *154*, 40−47.
(38) Wang, Y.; Zhang, C.; Zhao, L.; Meng, G.; Wu, J.; Liu, Z. Cellulose-based porous adsorbents with high capacity for methylene blue adsorption from aqueous solutions. *Fibers Polym.* **2017**, *18*, 891−899.
(39) Sharma, P. R.; Sharma, S. K.; Antoine, R.; Hsiao, B. S. Efficient removal of arsenic using zinc oxide nanocrystal-decorated regenerated microfibrillated cellulose scaffolds. *ACS Sustainable Chem. Eng.* **2019**, *7*, 6140−6151.
(40) Yang, R.; Su, Y.; Aubrecht, K. B.; Wang, X.; Ma, H.; Grubbs, R. B.; Hsiao, B. S.; Chu, B. Thiol-functionalized chitin nanofibers for As(III) adsorption. *Polymer* **2015**, *60*, 9−17.
(41) Ruan, C.; Strømme, M.; Lindh, J. A green and simple method for preparation of an efficient palladium adsorbent based on cysteine functionalized 2,3-dialdehyde cellulose. *Cellulose* **2016**, *23*, 2627−2638.
(42) Suopajärvi, T.; Liimatainen, H.; Hormi, O.; Niinimäki, J. Coagulation-flocculation treatment of municipal wastewater based on anionized nanocelluloses. *Chem. Eng. J.* **2013**, *231*, 59−67.
(43) Bruneel, D.; Schacht, E. Chemical modification of pullulan: 1. periodate oxidation. *Polymer* **1993**, *34*, 2628−2632.
(44) Maekawa, E.; Koshijima, T. Properties of 2,3-dicarboxy cellulose combined with various metallic ions. *J. Appl. Polym. Sci.* **1984**, *29*, 2289−2297.
(45) Keshk, S. M. A. S.; Ramadan, A. M.; Bondock, S. Physicochemical characterization of novel schiff bases derived from developed bacterial cellulose 2,3-dialdehyde. *Carbohydr. Polym.* **2015**, *127*, 246−251.

DOI: 10.1021/acsomega.9b03078
ACS Omega 2019, 4, 22008−22020

(46) Spuches, A. M.; Kruszyna, H. G.; Rich, A. M.; Wilcox, D. E. Thermodynamics of the As(III)−Thiol Interaction: Arsenite and Monomethylarsenite Complexes with Glutathione, Dihydrolipoic Acid, and Other Thiol Ligands. *Inorg. Chem.* **2005**, *44*, 2964−2972.
(47) Geng, B.; Wang, H.; Wu, S.; Ru, J.; Tong, C.; Chen, Y.; Liu, H.; Wu, S.; Liu, X. Surface-tailored nanocellulose aerogels with thiol-functional moieties for highly efficient and selective removal of Hg(II) ions from water. *ACS Sustainable Chem. Eng.* **2017**, *5*, 11715−11726.
(48) Sharma, P. R.; Joshi, R.; Sharma, S. K.; Hsiao, B. S. A simple approach to prepare carboxycellulose nanofibers from untreated biomass. *Biomacromolecules* **2017**, *18*, 2333−2342.
(49) Saito, T.; Kimura, S.; Nishiyama, Y.; Isogai, A. Cellulose nanofibers prepared by TEMPO-mediated oxidation of native cellulose. *Biomacromolecules* **2007**, *8*, 2485−2491.
(50) Saito, T.; Nishiyama, Y.; Putaux, J.-L.; Vignon, M.; Isogai, A. Homogeneous suspensions of individualized microfibrils from TEMPO-catalyzed oxidation of native cellulose. *Biomacromolecules* **2006**, *7*, 1687−1691.
(51) Fan, Y.; Saito, T.; Isogai, A. Chitin Nanocrystals Prepared by TEMPO-Mediated Oxidation of α-Chitin. *Biomacromolecules* **2008**, *9*, 192−198.
(52) Saito, T.; Okita, Y.; Nge, T. T.; Sugiyama, J.; Isogai, A. TEMPO-mediated oxidation of native cellulose: Microscopic analysis of fibrous fractions in the oxidized products. *Carbohydr. Polym.* **2006**, *65*, 435−440.
(53) Shinoda, R.; Saito, T.; Okita, Y.; Isogai, A. Relationship between length and degree of polymerization of TEMPO-oxidized cellulose nanofibrils. *Biomacromolecules* **2012**, *13*, 842−849.
(54) Da Silva Perez, D.; Montanari, S.; Vignon, M. R. TEMPO-mediated oxidation of cellulose III. *Biomacromolecules* **2003**, *4*, 1417−1425.
(55) Saito, T.; Isogai, A. TEMPO-mediated oxidation of native cellulose. The effect of oxidation conditions on chemical and crystal structures of the water-insoluble fractions. *Biomacromolecules* **2004**, *5*, 1983−1989.
(56) Sharma, P. R.; Varma, A. J. Thermal stability of cellulose and their nanoparticles: Effect of incremental increases in carboxyl and aldehyde groups. *Carbohydr. Polym.* **2014**, *114*, 339−343.
(57) Sharma, P. R.; Varma, A. J. Functionalized celluloses and their nanoparticles: Morphology, thermal properties, and solubility studies. *Carbohydr. Polym.* **2014**, *104*, 135−142.
(58) Sharma, P. R.; Rajamohanan, P. R.; Varma, A. J. Supramolecular transitions in native cellulose-I during progressive oxidation reaction leading to quasi-spherical nanoparticles of 6-carboxycellulose. *Carbohydr. Polym.* **2014**, *113*, 615−623.
(59) Lindh, J.; Carlsson, D. O.; Strømme, M.; Mihranyan, A. Convenient one-pot formation of 2,3-dialdehyde cellulose beads via periodate oxidation of cellulose in water. *Biomacromolecules* **2014**, *15*, 1928−1932.
(60) Rowen, J. W.; Forziati, F. H.; Reeves, R. E. Spectrophotometric Evidence for the Absence of Free Aldehyde Groups in Periodate-oxidized Cellulose. *J. Am. Chem. Soc.* **1951**, *73*, 4484−4487.
(61) Spedding, H. 628. Infrared spectra of periodate-oxidised cellulose. *J. Chem. Soc. (Resumed)* **1960**, 3147−3152.
(62) Duong, P. H. H.; Kuehl, V. A.; Mastorovich, B.; Hoberg, J. O.; Parkinson, B. A.; Li-Oakey, K. D. Carboxyl-functionalized covalent organic framework as a two-dimensional nanofiller for mixed-matrix ultrafiltration membranes. *J. Membr. Sci.* **2019**, *574*, 338−348.
(63) Rånby, B. G.; Hadler, E.; Åkerström, Å.; Finsnes, E.; Sörensen, J. S.; Sörensen, N. A. The Mercerisation of Cellulose. I. A Thermodynamic Discussion. *Acta Chem. Scand.* **1952**, *6*, 101−115.
(64) Atalla, R. H.; VanderHart, D. L. The role of solid state NMR spectroscopy in studies of the nature of native celluloses. *Solid State Nucl. Magn. Reson.* **1999**, *15*, 1−19.
(65) Segal, L.; Creely, J. J.; Martin, A. E.; Conrad, C. M. An empirical method for estimating the degree of crystallinity of native cellulose using the X-Ray diffractometer. *Text. Res. J.* **1959**, *29*, 786−794.
(66) Tan, C.; Li, L.; Zhong, D.-p.; Wang, H.; Li, K.-z. Separation of arsenic and antimony from dust with high content of arsenic by a selective sulfidation roasting process using sulfur. *Trans. Nonferrous Met. Soc. China* **2018**, *28*, 1027−1035.
(67) Guńka, P. A.; Dranka, M.; Piechota, J.; Żukowska, G. Z.; Zalewska, A.; Zachara, J. As_2O_3 polymorphs: theoretical insight into their stability and ammonia templated claudetite II crystallization. *Cryst. Growth Des.* **2012**, *12*, 5663−5670.
(68) Isogai, A.; Saito, T.; Fukuzumi, H. TEMPO-oxidized cellulose nanofibers. *Nanoscale* **2011**, *3*, 71−85.
(69) Biswal, B.; Kumar, S.; Singh, R. K. Production of hydrocarbon liquid by thermal pyrolysis of paper cup waste. *J. Waste Manage.* **2013**, *2013*, 1−7.
(70) Sahari, J.; Sapuan, S. M.; Zainudin, E. S.; Maleque, M. A. Mechanical and thermal properties of environmentally friendly composites derived from sugar palm tree. *Mater. Des.* **2013**, *49*, 285−289.
(71) Alemdar, A.; Sain, M. Biocomposites from wheat straw nanofibers: Morphology, thermal and mechanical properties. *Compos. Sci. Technol.* **2008**, *68*, 557−565.
(72) Fukuzumi, H.; Saito, T.; Iwata, T.; Kumamoto, Y.; Isogai, A. Transparent and high gas barrier films of cellulose nanofibers prepared by TEMPO-mediated oxidation. *Biomacromolecules* **2009**, *10*, 162−165.
(73) Gomez-Bujedo, S.; Fleury, E.; Vignon, M. R. Preparation of cellouronic acids and partially acetylated cellouronic acids by TEMPO/NaClO oxidation of water-soluble cellulose acetate. *Biomacromolecules* **2004**, *5*, 565−571.
(74) Fukuzumi, H.; Saito, T.; Okita, Y.; Isogai, A. Thermal stabilization of TEMPO-oxidized cellulose. *Polym. Degrad. Stab.* **2010**, *95*, 1502−1508.
(75) Jakab, E.; Mészáros, E.; Borsa, J. Effect of slight chemical modification on the pyrolysis behavior of cellulose fibers. *J. Anal. Appl. Pyrolysis* **2010**, *87*, 117−123.
(76) Kim, U.-J.; Kuga, S. Thermal decomposition of dialdehyde cellulose and its nitrogen-containing derivatives. *Thermochim. Acta* **2001**, *369*, 79−85.
(77) Weiss, I. M.; Muth, C.; Drumm, R.; Kirchner, H. O. K. Thermal decomposition of the amino acids glycine, cysteine, aspartic acid, asparagine, glutamic acid, glutamine, arginine and histidine. *BMC Biophys.* **2018**, *11*, 2.
(78) Freundlich, H. Über die adsorption in lösungen. *Z. Phys. Chem.* **1907**, *57U*, 385−470.
(79) Eguez, H. E.; Cho, E. H. Adsorption of arsenic on activated charcoal. *J. Miner. Met. Mater. Soc.* **1987**, *39*, 38−41.
(80) Gupta, K.; Ghosh, U. C. Arsenic removal using hydrous nanostructure iron(III)−titanium(IV) binary mixed oxide from aqueous solution. *J. Hazard. Mater.* **2009**, *161*, 884−892.
(81) Raven, K. P.; Jain, A.; Loeppert, R. H. Arsenite and Arsenate Adsorption on Ferrihydrite: Kinetics, Equilibrium, and Adsorption Envelopes. *Environ. Sci. Technol.* **1998**, *32*, 344−349.
(82) Zhao, Z.; Liu, J.; Cui, F.; Feng, H.; Zhang, L. One pot synthesis of tunable Fe_3O_4−MnO_2 core−shell nanoplates and their applications for water purification. *J. Mater. Chem.* **2012**, *22*, 9052−9057.
(83) Sun, T.; Zhao, Z.; Liang, Z.; Liu, J.; Shi, W.; Cui, F. Efficient As(III) removal by magnetic CuO−Fe_3O_4 nanoparticles through photo-oxidation and adsorption under light irradiation. *J. Colloid Interface Sci.* **2017**, *495*, 168−177.
(84) Styles, P. M.; Chanda, M.; Rempel, G. L. Sorption of arsenic anions onto poly(ethylene mercaptoacetimide). *React. Funct. Polym.* **1996**, *31*, 89−102.
(85) Matsunaga, H.; Yokoyama, T.; Eldridge, R. J.; Bolto, B. A. Adsorption characteristics of arsenic(III) and arsenic(V) on iron(III)-loaded chelating resin having lysine-Nα,Nα-diacetic acid moiety. *React. Funct. Polym.* **1996**, *29*, 167−174.

DOI: 10.1021/acsomega.9b03078
ACS Omega 2019, 4, 22008−22020